Best integer equivariant estimation

performance analysis using real data collected by low-cost, single- and dual-frequency, multi-GNSS receivers for short- to long-baseline RTK positioning

Odolinski, Robert; Teunissen, Peter J.G.

DOI
10.1007/s00190-020-01423-2

Publication date
2020

Document Version
Final published version

Published in
Journal of Geodesy

Journal of Geodesy (2020) 94:91
https://doi.org/10.1007/s00190-020-01423-2

ORIGINAL ARTICLE

Best integer equivariant estimation: performance analysis using real data collected by low-cost, single- and dual-frequency, multi-GNSS receivers for short- to long-baseline RTK positioning

Robert Odolinski[1] · **Peter J. G. Teunissen**[2,3]

Received: 3 May 2020 / Accepted: 12 August 2020

Abstract
The key to precise global navigation satellite system (GNSS) positioning is carrier phase integer ambiguity resolution with a high success rate. On the other hand when the success rate is too low, the user will normally prefer the float solution. The alternative can be to use the best integer equivariant (BIE) estimator, since it is optimal in the minimum mean squared error (MMSE) sense. Low-cost receiver real-time kinematic precise positioning has become possible through the many signals that can be obtained by combining several GNSSs, such as BDS, Galileo, QZSS and GPS. In this contribution, we will use both simulations and such low-cost multi-GNSS data to compare the performance of the BIE and integer least squares (ILS) estimator, based on full ambiguity resolution. The GNSS data are evaluated in Dunedin, New Zealand, with a short- (670 m) and long-baseline (112.9 km) where the relative atmospheric delays can be neglected and need to be estimated, respectively. We compare the BIE and ILS results by using both single-frequency and dual-frequency (DF) low-cost and survey-grade receivers and antennas. We demonstrate, for the first time, the distributional properties of BIE positioning, where it will be shown that a 'star-like' pattern reveals itself once the model gets stronger and the ILS success rate increases. It will further be shown that the DF low-cost receivers give a very good positioning performance, but still not yet competitive to the survey-grade counterparts for the long-baseline. We will also demonstrate that the positioning performance of the BIE estimator will always equal or be better than that of the float solutions. It will finally be shown that BIE will always be better in the MMSE sense than the ILS solution when the success rate is at low to medium levels, whereas for high success rates we get a similar performance to ILS.

Keywords Best integer equivariant (BIE) estimator · Integer least squares (ILS) estimator · Low-cost receiver · Low-cost antenna · Single-frequency (SF) · Dual-frequency (DF) · Real-time kinematic (RTK) positioning

1 Introduction

Carrier-phase integer ambiguity resolution is the key to high precision global navigation satellite system (GNSS) real-time kinematic (RTK) positioning. The combination of several GNSSs like the Russian GLONASS, Chinese BeiDou Navigation Satellite System (BDS), European Galileo, Japanese Quasi-Zenith Satellite System (QZSS) and American Global Positioning System (GPS) has also made low-cost receiver (Odolinski and Teunissen 2016; Mongredien et al. 2016; Odolinski and Teunissen 2017b) and smartphone precise positioning possible (Riley et al. 2017; Zhang et al. 2018; Odolinski and Teunissen 2019; Paziewski et al. 2019; Aggrey et al. 2020; Nie et al. 2020).

The method to obtain RTK-derived positions is to fix the full or partial (Teunissen et al. 1999; Brack and Gunther 2014; Brack 2015, 2017) integer vector when the corresponding ambiguity success rate is very high (Teunissen 1995). On the other hand when the success rate is low, one usually opts for the float solution. The alternative is to use the best integer equivariant (BIE) estimator as introduced

✉ Robert Odolinski
Robert.Odolinski@otago.ac.nz

Peter J. G. Teunissen
P.J.G.Teunissen@tudelft.nl

[1] National School of Surveying, University of Otago, Dunedin, New Zealand

[2] Department of Spatial Sciences, GNSS Research Centre, Curtin University of Technology, Perth, Australia

[3] Department of Geoscience and Remote Sensing, Delft University of Technology, Delft, The Netherlands

Published online: 02 September 2020

by Teunissen (2003b). This estimator is optimal in the minimum mean squared errors (MSEs) sense, and it has the added advantage that no separate ambiguity validation step is needed as is the case when using integer estimators such as the integer least squares (ILS) estimator (Teunissen 2003b; Verhagen and Teunissen 2005; Brack 2019). Verhagen and Teunissen (2005), Brack et al. (2014), Brack (2019) used simulation to study the distributional properties and performance of the BIE estimator when compared to the float and ILS fixed counterparts. Laurichesse and Banville (2018) used BIE for instantaneous, cm-level, precise point positioning (PPP) while making use of survey-grade, multi-frequency receivers.

In this contribution, we study the BIE performance using simulations as well as real data collected by low-cost, multi-GNSS, single-frequency (SF) and dual-frequency (DF) RTK receivers and antennas. With 'low-cost', we refer to the combined cost of SF and DF receivers and antennas of at most a few hundred USDs. We will also, for the first time, reveal the 'star-like' distribution in the positioning-space rather than the low-dimensional ambiguity space (Verhagen 2005). All BIE results will be compared to that of the float and ILS solutions, based on full ambiguity resolution. In Sect. 2, we define our functional model and show how the standard ILS ambiguity and baseline solution is derived. In this section, we also describe the BIE estimator. In Sect. 3, we then describe the Monte Carlo simulations and compare these results to real multi-GNSS data collected through a short-baseline (670 m) while employing low-cost SF receivers and antennas. In Sect. 4, we show BIE results for simulated data and real multi-GNSS data collected through a long-baseline (112.9 km) with low-cost DF receivers and antennas. Performance comparisons are here also made to that of survey-grade receivers and antennas. With short- and long-baselines, we refer to the case where the ionospheric and tropospheric delays can be assumed absent and need to be modeled as completely unknown parameters, respectively. Finally in Sect. 5, we end up with a summary and conclusions.

2 Best integer equivariant estimation for the multi-frequency, multi-system RTK model

2.1 Multi-frequency and multi-system RTK model

In the following system of observation equations, we assume that we have access to DF and double-differenced (DD) code and phase data of GPS, BDS, Galileo and QZSS. When we refer to BDS, we refer to the BDS-2 regional system (Odolinski et al. 2013; Yang et al. 2014) and not the new global BDS-3 constellation (Yang et al. 2019). The satellite orbits and clocks are obtained through the broadcast ephemeris, and we omit time stamps for brevity. We take a common reference satellite on the overlapping frequencies between the systems to further strengthen the model. Since throughout our results we are using similar receiver types, with the same firmware version, modeling of the inter-system biases (ISBs) on the overlapping frequencies is safely neglected (Odijk and Teunissen 2013; Odolinski and Teunissen 2017a, 2019). The linearized DD system of observation equations read,

$$E(y) = Aa + Bb,\ a \in \mathbb{Z}^n, b \in \mathbb{R}^p \tag{1}$$

where $E(.)$ is the expectation operator, y the vector of code and phase observations of size m, a is the n vector of unknown integer ambiguities, and b the p vector of real-valued baseline components (and for sufficiently long baselines, it also includes relative ionospheric and tropospheric delays). The design matrices A and B are of size $m \times n$ and $m \times p$, respectively, and are assumed to be of full rank.

2.2 Integer least squares estimation

The GNSS model (1) is solved in the following three-step procedure (Teunissen 1995).

2.2.1 The float solution

Firstly, we assume the ambiguities to be real-valued parameters $a \in \mathbb{R}^n$ and perform a least squares (LS) adjustment (Teunissen 2003a), so as to obtain the so-called float solution of the ambiguities and baseline components, denoted with a 'hat', as,

$$\begin{aligned} \hat{a} &= \left(\overline{A}^T Q_{yy}^{-1} \overline{A}\right)^{-1} \overline{A}^T Q_{yy}^{-1} y \\ \hat{b} &= \left(B^T Q_{yy}^{-1} B\right)^{-1} B^T Q_{yy}^{-1} \left(y - A\hat{a}\right) \end{aligned} \tag{2}$$

with $\overline{A} = P_B^{\perp} A$, and the orthogonal projector defined as $P_B^{\perp} = I_m - B\left(B^T Q_{yy}^{-1} B\right)^{-1} B^T Q_{yy}^{-1}$, where Q_{yy} is the variance (vc) matrix, i.e., the stochastic model, of the DD code and phase observations, with an exponential elevation-dependent weight employed for each satellite (Euler and Goad 1991). The float vc matrices of the ambiguities and baseline components in (2) read,

$$\begin{aligned} Q_{\hat{a}\hat{a}} &= \left(\overline{A}^T Q_{yy}^{-1} \overline{A}\right)^{-1} \\ Q_{\hat{b}\hat{b}} &= \left(\overline{B}^T Q_{yy}^{-1} \overline{B}\right)^{-1} \end{aligned} \tag{3}$$

with $\overline{B} = P_A^{\perp} B$ and $P_A^{\perp} = I_m - A\left(A^T Q_{yy}^{-1} A\right)^{-1} A^T Q_{yy}^{-1}$. The second step is to solve the ILS problem making use of the float ambiguities $\hat{a} \in \mathbb{R}^n$ in (2) and search for its corresponding integer solution $a \in \mathbb{Z}^n$.

2.2.2 Integer ambiguity estimation

Different integer estimators exist, such as those of Integer Rounding, Integer Bootstrapping and integer least squares (ILS). Here, we choose ILS as it is optimal in the sense of having the largest possible success-rate of all integer estimators (Teunissen 1999a). The ILS ambiguity estimator is denoted with a 'check' and defined as,

$$\check{a} = \underset{a\in\mathbb{Z}^n}{\arg\min} ||\hat{a} - a||^2_{Q_{\hat{a}\hat{a}}} \tag{4}$$

where $||.||^2_{Q_{\hat{a}\hat{a}}} = (.)^T Q^{-1}_{\hat{a}\hat{a}}(.)$. This ILS problem is then efficiently solved by means of the LAMBDA method (Teunissen 1995; De Jonge and Tiberius 1996).

2.2.3 Fixed solution

In the third step, we compute the fixed baseline solution as,

$$\check{b} = \hat{b} - Q_{\hat{b}\hat{a}} Q^{-1}_{\hat{a}\hat{a}} \left(\hat{a} - \check{a}\right) \tag{5}$$

Provided the uncertainty in $\check{a}$ can be neglected, we have,

$$Q_{\check{b}\check{b}} = Q_{\hat{b}\hat{b}} - Q_{\hat{b}\hat{a}} Q^{-1}_{\hat{a}\hat{a}} Q_{\hat{a}\hat{b}} < Q_{\hat{b}\hat{b}} \tag{6}$$

where $Q^T_{\hat{b}\hat{a}} = Q_{\hat{a}\hat{b}}$ are the float covariance matrices. As the precision of the fixed baseline is driven by the very-precise carrier-phase data, while that of $\hat{b}$ in the single-epoch case merely by the pseudorange data, the standard deviations of $\check{b}$ will then be a two-order of magnitude smaller than those of $\hat{b}$. However, for this to hold true, the uncertainty in the resolved integer ambiguities must be negligible, implying that their success rate (i.e., probability of correct integer estimation) should be sufficiently close to one.

2.3 Best integer equivariant estimation

On the other hand, when the success rate is too low, the user will normally prefer the float $\hat{b}$ rather than the fixed solution $\check{b}$ in (5). The alternative in such cases can be to use the BIE estimator (Teunissen 2003b) to solve for the ambiguities. Assuming normally distributed data, the BIE estimator denoted with 'overline' is given as,

$$\overline{a} = \sum_{z\in\mathbb{Z}^n} z \frac{\exp\left(-\frac{1}{2}\|\hat{a} - z\|^2_{Q_{\hat{a}\hat{a}}}\right)}{\sum_{z\in\mathbb{Z}^n}\exp\left(-\frac{1}{2}\|\hat{a} - z\|^2_{Q_{\hat{a}\hat{a}}}\right)} \tag{7}$$

The BIE baseline solution can then be derived as,

$$\overline{b} = \hat{b} - Q_{\hat{b}\hat{a}} Q^{-1}_{\hat{a}\hat{a}} \left(\hat{a} - \overline{a}\right) \tag{8}$$

where the ILS solution $\check{a}$ in (5) has been replaced by the BIE solution $\overline{a}$ computed in (7). It was proven by Teunissen (2003b) that the BIE estimator is unbiased and that it minimizes the mean squared errors (MSEs) in the class of integer equivariant (IE) estimators. And since it was also shown in (ibid) that the IE-class includes the class of integer-estimators, as well as the class of linear estimators, the mean squared error of the BIE estimator is also always smaller than that of the ILS estimator and float LS estimator. We therefore have:

$$\begin{aligned} D\left(\overline{b}\right) &\leq D\left(\check{b}\right) \\ D\left(\overline{b}\right) &\leq D\left(\hat{b}\right) \end{aligned} \tag{9}$$

where $D(.)$ is the dispersion operator. The BIE estimator becomes similar to the ILS solution when the success rate is very high, and similar to the float solution when the success rate is very low (Teunissen 2003b).

Note that the BIE solution in (7) involves an infinite weighted sum over the whole space of integers, which is computationally impractical. Teunissen (2005) has shown that one can make use of a finite integer set $\Theta^\lambda_{\hat{a}}$ while still maintaining the property of integer-equivariance,

$$\overline{a}^\lambda = \sum_{z\in\Theta^\lambda_{\hat{a}}} z \frac{\exp\left(-\frac{1}{2}\|\hat{a} - z\|^2_{Q_{\hat{a}\hat{a}}}\right)}{\sum_{z\in\Theta^\lambda_{\hat{a}}}\exp\left(-\frac{1}{2}\|\hat{a} - z\|^2_{Q_{\hat{a}\hat{a}}}\right)} \tag{10}$$

where $z \in \mathbb{Z}^n$ in (7) has been replaced by $z \in \Theta^\lambda_{\hat{a}}$ in (10). The integers that reside in the set $\Theta^\lambda_{\hat{a}}$ depends then on the ellipsoidal region around the float solution $\hat{a}$ with its radius defined in the metric of $Q_{\hat{a}\hat{a}}$, which can be defined as follows (Teunissen 2005),

$$\|\hat{a} - z\|^2_{Q_{\hat{a}\hat{a}}} < \lambda^2 \tag{11}$$

where the threshold λ^2 can be determined from a central Chi-squared distribution χ^2 with n degrees of freedom and a small significance level α. In this article, we choose $\alpha = 10^{-9}$ to avoid any computational burden, which produces near-identical results as the setting of $\alpha = 10^{-16}$, similar to Verhagen (2005). We also remark that again the LAMBDA method is used to efficiently find the integer vectors residing in the ellipsoidal region (11).

In the following sections, we will evaluate how the BIE performance (9) hold true for the BIE approximation in (10), while using real data collected by low-cost SF and DF multi-GNSS receivers and antennas in Dunedin, NZ.

Table 1 Undifferenced and zenith-referenced STDs for code and phase with simulated data and a SF L1 GPS model, with an elevation cut-off angle of 10° and 11 satellites (see skyplot in Fig. 1)

$\hat{\sigma}_{p_1}$ (cm)	$\hat{\sigma}_{\phi_1}$ (mm)	L1 ILS SR (%)
50	5.0	11.8
37	3.7	40.8
25	2.5	83.5
20	2.0	94.1
18	1.8	96.6
15	1.5	99.0
10	1.0	100.0

The corresponding single-epoch L1 ILS SRs are given in the last column

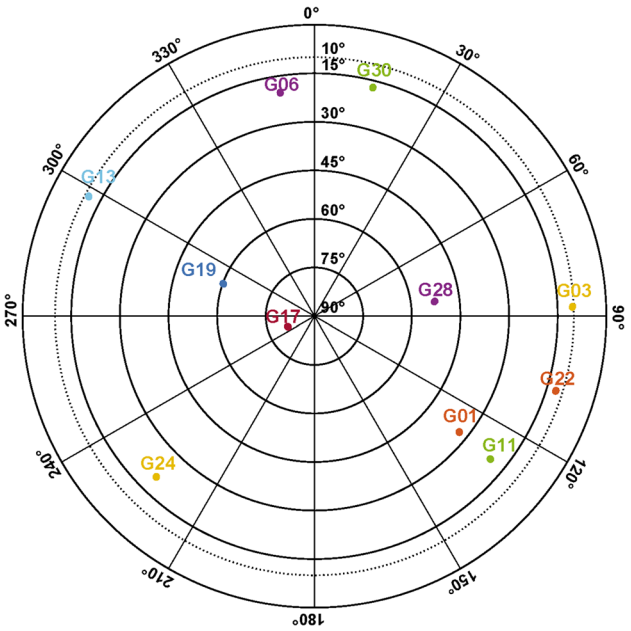

Fig. 1 Skyplot of L1 GPS with an elevation cut-off angle of 10° for the simulated data from a position in Dunedin, NZ

3 BIE for single-epoch and short-baseline SF RTK positioning

3.1 BIE simulation for single-epoch SF L1 GPS RTK positioning

To better understand the real data results to be presented in the following section, we will in this section present results for simulated data with a fixed satellite geometry. In order to do this, we make use of Monte Carlo simulations, where the code and phase observations are produced using the zenith-referenced and undifferenced standard deviations (STDs) in Table 1 together with an exponential elevation weighting function (Euler and Goad 1991). In the single-baseline RTK model (1), we assume any residual atmospheric delays to be absent (here referred to as the 'ionosphere-fixed' model); hence, the results presented here hold true for a short baseline. Table 1 shows also the corresponding single-epoch ILS success rates (SRs). The SF L1 GPS satellite constellation in Fig. 1 is used as obtained through the broadcast ephemeris for a position in Dunedin, NZ. We simulate 200,000 samples of observations, where the benchmark coordinates and satellite coordinates of the broadcast ephemeris are assumed to be true coordinates. This has as a consequence that the estimated receivers coordinates will be unbiased, and thus the mean of the positioning errors to be depicted will be zero.

Figure 2 depicts simulated horizontal (North and East) single-epoch, ambiguity-float, ILS and BIE SF ionosphere-fixed positioning errors as black, magenta and green dots, respectively. The ILS positioning results follow a multi-modal continuous probability density function (PDF), see further Fig. 3, and thus all the ILS solutions that have the same integer ambiguity vector are classified into different clusters if they exceed a certain number of positioning solutions. A cluster of $\geq$ 5000 positioning solutions is denoted as the largest magenta dot, where the corresponding number for the second largest magenta dots, etc., is 500 to $<$ 5000, 50 to $<$ 500, 5 to $<$ 50, and finally a single ILS solution. The top to bottom row and from left to right panels show models with an ILS SR of 11.8%, 40.8%, 83.5%, 94.1%, 99.0% and 100.0%, respectively. The zoom-in window is depicted to show the two-order of magnitude improvement when going from ambiguity-float, to successfully fixing the ambiguities to their correct integer values through ILS. Note that in this zoom-in window all ILS solutions are shown as their single-epoch ILS solutions (small magenta dots).

Figure 3 shows a selection of the corresponding histograms of the North positioning errors in Fig. 2, where the left column panels depict the ILS, the middle column BIE, and the right column the ambiguity-float positioning results. The East and Up positioning errors behave in a similar manner and are thus not depicted for brevity. On top of the float solutions, we also plot the theoretical normal distribution, and we use kernel smoothing (Wand and Jones 1995) to fit a distribution to the BIE results and the ILS solutions in the zoom-in windows. The zoom-in windows show that the ILS solutions follow indeed a multi-modal and continuous PDF (Teunissen 1999b), and that the stronger the model strength, i.e., the higher the ILS SR, the more peaked the distribution becomes around zero meters. We remark that the y-axis for the zoom-in windows are different between each row, so that a direct comparison can be made between ILS, BIE and ambiguity-float solutions for each model strength.

Figure 2 and the top left panel show that with a lower SR (in this case 11.8% ILS SR) the precision of the BIE solutions resembles that of the float solutions, which is depicted as green dots that generally are plotted above or very close to the black dots, respectively. This is also illustrated through

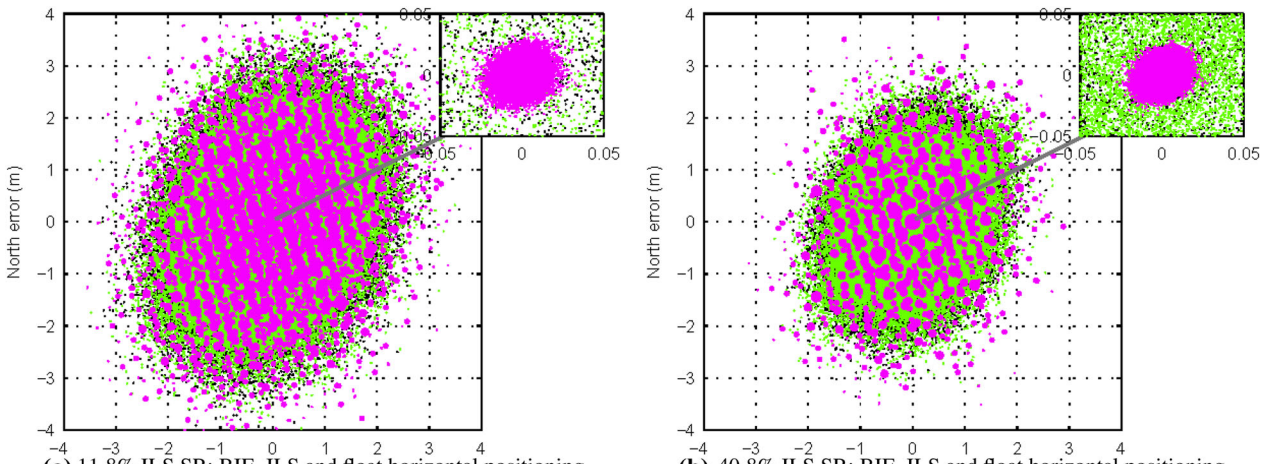

(a) 11.8% ILS SR: BIE, ILS and float horizontal positioning

(b) 40.8% ILS SR: BIE, ILS and float horizontal positioning

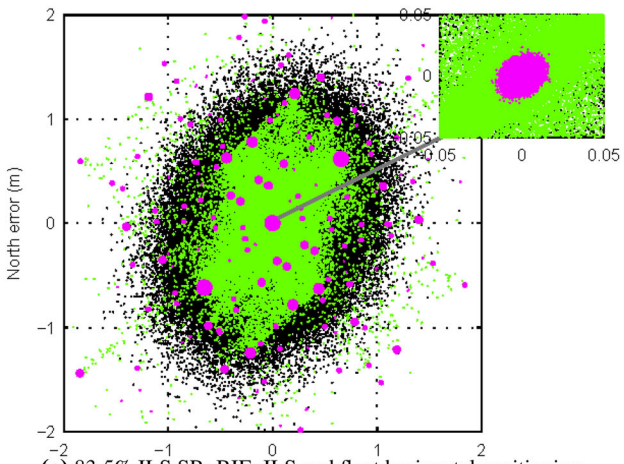

(c) 83.5% ILS SR: BIE, ILS and float horizontal positioning.

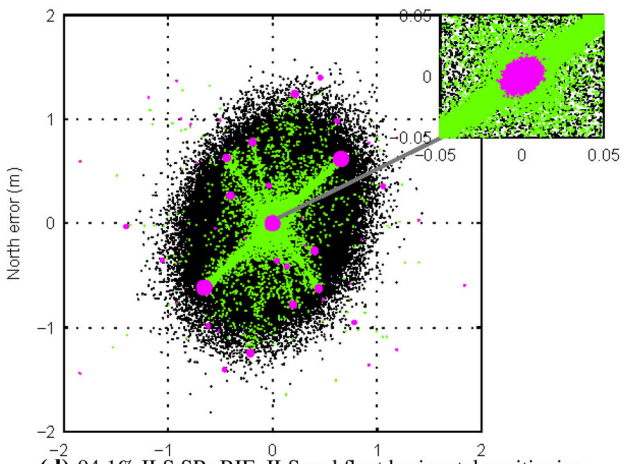

(d) 94.1% ILS SR: BIE, ILS and float horizontal positioning

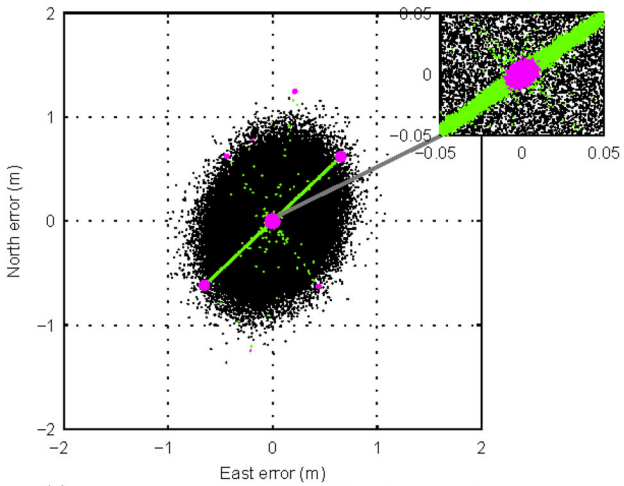

(e) 99.0% ILS SR: BIE, ILS and float horizontal positioning

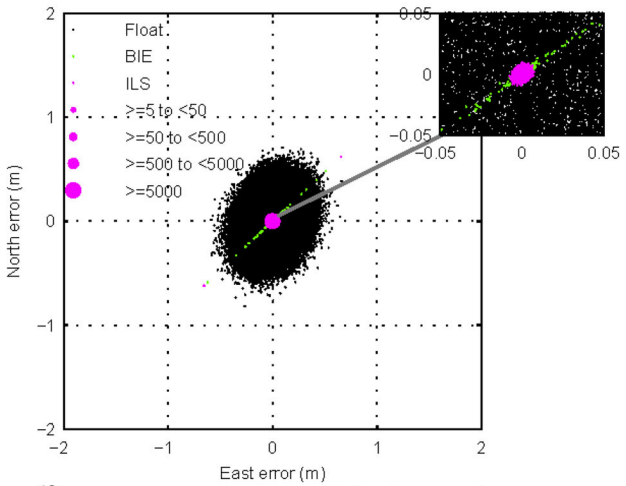

(f) 100.0% ILS SR: BIE, ILS and float horizontal positioning

Fig. 2 Simulated (200,000 samples, see Table 1 and Fig. 1) horizontal (North/East) scatter of the BIE (*green dots*), ILS (*magenta dots*), and ambiguity-float (*black dots*) ionosphere-fixed SF L1 GPS (cut-off 10°) RTK positioning errors. The largest magenta dots are for ILS positioning solutions that have the same integer ambiguity vector and exceeds a cluster of $\geq$ 5000 positioning solutions, where the corresponding number for the second largest magenta dots, etc., are 500 to $<$ 5000, 50 to $<$ 500, 5 to $<$ 50 and a single ILS solution. This multi-modal distribution of the ILS solutions is also depicted by the histograms in Fig. 3. Note the x- and y-axis scale difference between the two weakest models at the top row and all other solutions

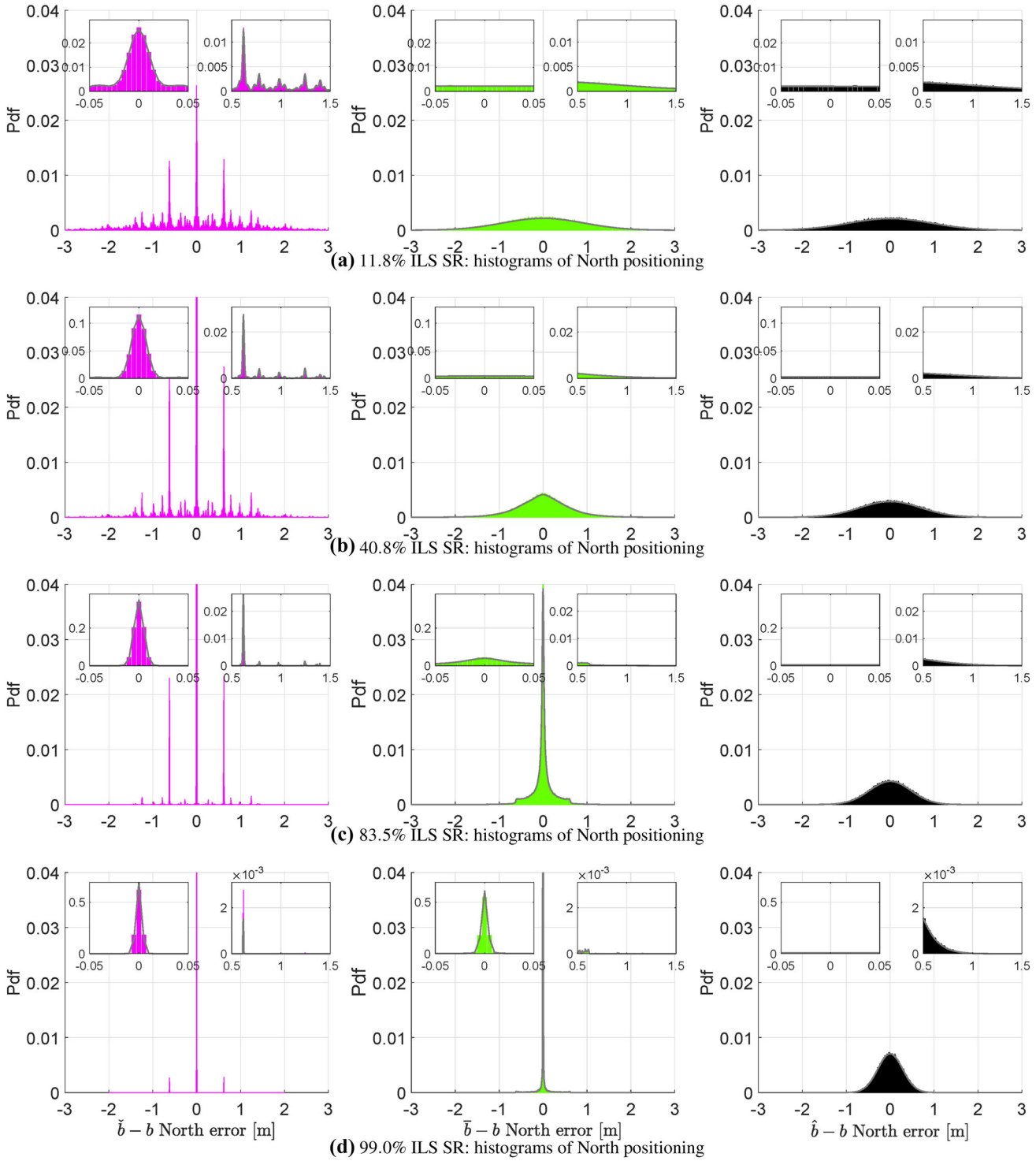

(a) 11.8% ILS SR: histograms of North positioning

(b) 40.8% ILS SR: histograms of North positioning

(c) 83.5% ILS SR: histograms of North positioning

(d) 99.0% ILS SR: histograms of North positioning

Fig. 3 Example histograms (bin size of 5 mm) of simulated (200,000 samples, see Table 1 and Fig. 1) North positioning errors in Fig. 2 of the BIE (*green bars*), ILS (*magenta bars*) and ambiguity-float (*black bars*) solutions. The East and Up positioning histograms behave in a similar manner and are thus not shown for brevity. The theoretical normal distribution is plotted for the float solutions, and kernel smoothing (Wand and Jones 1995) is used to fit a distribution to the BIE solutions and ILS solutions depicted in the zoom-in windows, respectively, which are all given as *gray lines*. The zoom-in windows depict the spread of the sample solutions of North errors between −0.05 and 0.05 m and 0.5 to 1.5 m, respectively

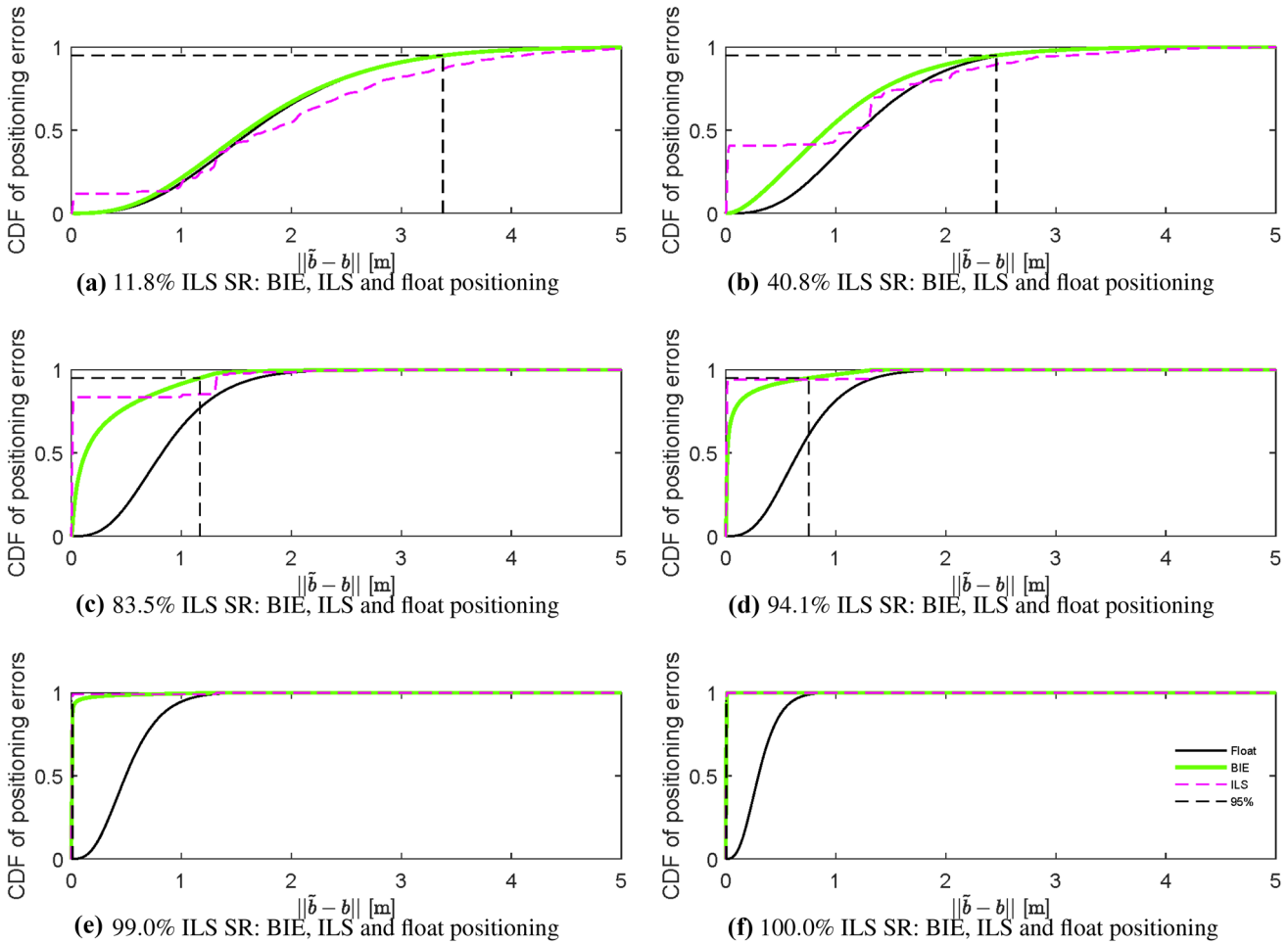

(a) 11.8% ILS SR: BIE, ILS and float positioning
(b) 40.8% ILS SR: BIE, ILS and float positioning
(c) 83.5% ILS SR: BIE, ILS and float positioning
(d) 94.1% ILS SR: BIE, ILS and float positioning
(e) 99.0% ILS SR: BIE, ILS and float positioning
(f) 100.0% ILS SR: BIE, ILS and float positioning

Fig. 4 CDF of simulated (200,000 samples, see Table 1 and Fig. 1) BIE, ILS, ambiguity-float and ionosphere-fixed SF RTK positioning errors in Fig. 2. $\tilde{b}$ are either the float $\hat{b}$ (*black lines*), ILS $\check{b}$ (*magenta dashed lines*) and BIE $\overline{b}$ (*green lines*) estimated 3D coordinates, respectively, and ||.|| is the norm of this vector. The *dashed black line* corresponds to the 95% CI

their similar histograms that follow a theoretical normal distribution in Fig. 3. For all models in Fig. 2, we can see that the ILS solutions indeed follow a multi-modal distribution (c.f. Fig. 3), and that the majority of incorrect ILS solutions are generally located in the South-West and North-East direction due to the corresponding poorer satellite coverage (c.f. Fig. 1). The BIE solutions are then shown to become better than the float solutions when the ILS SR increases to, for example, 40.8% in the top right panel of Fig. 2, which is also indicated by the many more green dots visible in the zoom-in window (and plotted underneath the magenta dots). We can also see that when the model becomes much stronger, such as at the middle and bottom panels, we obtain fewer number of incorrectly fixed solutions. This gives rise to a 'star-like' scattering of the BIE solutions as they are computed as a (weighted) average of all integer vectors within the search space defined by (11). As the weight is larger, the closer the integer vector is to the float solution in the metric of the ambiguity variance matrix, the more the 'star' symmetry will point in the directions of integer vectors that have a larger probability of being an ILS solution.

Finally, Fig. 2 shows also instances, for example in the middle left panel and for the scenario with an ILS SR of 83.5%, where frequent occurring ILS baseline solutions can be further apart from the correct solution than less frequent occurring ILS baseline solutions (c.f. Fig. 3). As expected, for instances when the distance between these ILS solutions and the float solutions is large, these incorrect ILS solutions are shown to not be as heavily weighted into the BIE solutions (since there are indeed fewer green dots pointed toward these locations). In other words, when the ILS SR is not sufficiently close to 100%, BIE will produce solutions that are less likely to be far from the true coordinates without the need to make use of integer validation techniques (see, e.g., Teunissen and Verhagen 2009). Also note that the model at bottom row and right column of Fig. 2 has a 99.997% ILS

SR (but here rounded to 100% ILS SR), which explains the few BIE solutions directed toward those incorrectly fixed ILS solutions.

Figure 3 and the top row show that when the model is weak (ILS SR of 11.8%), the BIE and ambiguity-float solutions, in the two right columns, have, as expected, similar positioning precisions and follow well a theoretical normal distribution. Once the model gets stronger, however, as shown at the second row (ILS SR 40.8%), the BIE distribution gets more peaked than that of the float distribution which indicates an overall better positioning precision. For the same models, we can also see, e.g., in the histogram zoom-in of Fig. 3, that ILS (in the left column) has more instances than BIE with large North positioning errors of say above 0.5 m. For example, the highest PDF peak for ILS is almost 3% with errors above 0.5 m as shown in the second row of Fig. 3, whereas BIE has a much smaller PDF value for the similar magnitude of positioning error. Note also that the ILS solutions are here indeed multi-modal distributed (and symmetric with respect to zero meters), but that the corresponding distribution gets more peaked for both zoom-in windows when going from the weakest model at the top row, to a stronger model at the second row. This trend follows accordingly when the ILS SR increases to 83.5% and 99.0% at the bottom two rows, respectively. Most importantly for these two stronger models, we can also see that the BIE distribution gets even more peaked than the float solution, and at the same time it has again fewer instances than ILS of positioning errors of say above 0.5 m and below -0.5 m, respectively. Finally, when we have an ILS SR of 99.0% at the bottom row, it is shown that the BIE PDF resembles indeed that of ILS.

Figure 4 shows the cumulative distribution function (CDF) of the 3D BIE, ILS and ambiguity-float positioning results. The black lines corresponds to the float, magenta dashed lines to the ILS, green lines to the BIE positioning solutions, and dashed black lines to 95% confidence intervals (CI). The vector $\tilde{b}$ is either the float $\hat{b}$, ILS $\check{b}$ and BIE $\bar{b}$ estimated 3D coordinates, respectively, and $||.||$ denotes the unweighted L2-norm of this vector.

Similarly to Figs. 2 and 3, we can see in top row of Fig. 4, for the weakest model with the lowest ILS SR (11.8%), that the BIE solutions resemble indeed that of the float solutions ($||\hat{b} - b||$), and for an ILS SR of 100% at bottom row and right column it equals the ILS estimator (c.f. Fig. 2). The CDF ILS ($||\check{b} - b||$) stepwise function (magenta dashed lines) in the top two rows indicates that if $\check{b}$ is not close to b, it will immediately be far from the true baseline (due to its multi-modal distribution, c.f. Fig. 3), whereas for BIE (CDF of $||\bar{b} - b||$) this is not necessarily the case. For instance, if we focus our attention on the top row and right column of Fig. 4, the ILS CDF quickly reaches values close to its ILS SR (40.8%) for small positioning errors, and then the CDF goes quickly toward the one meter level before it significantly

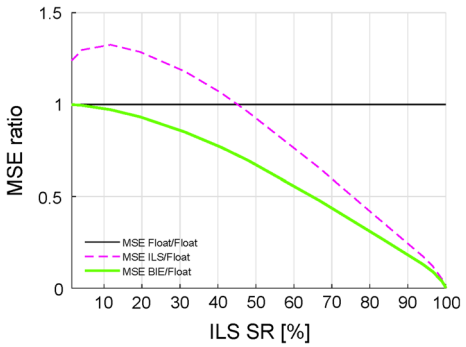

Fig. 5 MSE ratios of the simulated (200,000 samples, see Table 1 and Fig. 1) BIE (*green line*), ILS (*dashed magenta line*), ambiguity-float (*black line*) solutions, all versus float, for the ionosphere-fixed SF RTK positioning errors in Fig. 2

increases again. On the other hand, for the BIE estimator the CDF is larger than ILS for errors of say one meter for the top two rows of Fig. 4, but at the same time it is also less likely to have small positioning errors (except when the ILS SR is very high). Most importantly, we can see for all ILS SRs up to 94.1%, when one would not fix the ambiguities in practice, that the 95% CI of BIE is smaller than that of the ILS and smaller (or equal) to the float solutions.

Figure 5 depicts the MSEs ratios of BIE as green and ILS as a dashed magenta line, relative to the ambiguity-float solutions (float vs. float ratio is given as a black line). We simulated a few extra ILS SRs cases, in addition to the ones depicted in Table 1, to give a smoother behavior of the depicted ratios. Note that since the simulated positions are unbiased, the MSEs equal the sum of the variances of North, East and Up.

Figure 5 shows that ILS has a larger MSE than the float solutions for an ILS SR up to about 45%, and always larger than BIE until we reach an ILS SR of 100% (when they become similar). Finally, as the results show, the MSE of BIE is, with the exception when the ILS SR equals 0% or 100%, always better than that of the float and ILS-fixed solutions. For the 0% and 100% SR case, the BIE is identical to the float and ILS solution, respectively.

3.2 BIE for single-epoch SF RTK positioning with real multi-GNSS data

In order to validate the simulation results in the previous section, we will use 48 h (30 s measurement interval) of real data collected through low-cost ublox EVK-M8T receivers and patch antennas with SF GPS + Galileo + BDS + QZSS in Dunedin, NZ and a 670 m baseline. A circular ground plane was used for each patch antenna to reduce any multipath effects. The Detection, Identification and Adaptation (DIA) procedure by Teunissen (1990) was used to detect and identify outliers. The number of satellites of this data is depicted

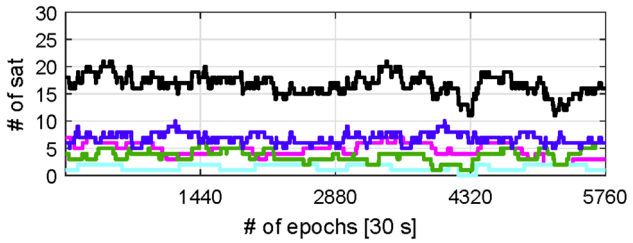

Fig. 6 Number of satellites for SF GPS+Galileo+BDS+QZSS with an elevation cut-off angle of 20° for the real multi-GNSS data collected in Dunedin, NZ. The *black lines* corresponds to a combined 4-system model, *blue lines* GPS, *green lines* Galileo, *magenta lines* BDS and *cyan lines* QZSS

Table 2 Undifferenced and zenith-referenced STDs for code and phase for a SF L1 + E1 + B1 + L1 GPS + Galileo + BDS + QZSS model (ublox + patch), with an elevation cut-off angle of 20° over 48 h (30 s) of real data collected in Dunedin, NZ at 5 Jan, 2018 from 05:00 (hh:mm) UTC

	$\hat{\sigma}_{p_j}$ (cm)	$\hat{\sigma}_{\phi_j}$ (mm)
L1 GPS	45	2
E1 Galileo	41	2
B1 BDS	58	2
L1 QZSS	48	2

in Fig. 6, where an elevation cut-off angle of 20° is mainly used so as to give similar ILS SRs to the simulation results in the previous section when combining different GNSSs. The stochastic model settings in Table 2 were used, as obtained through least-squares variance component estimation (LS-VCE) similar to Odolinski and Teunissen (2019). Making use of a realistic stochastic model is important as otherwise the float and ILS positioning performance would deteriorate. Since the BIE solutions are a (weighted) average of all ILS integer vectors within the search space defined by (11), the BIE performance would then worsen as well.

Figure 7 depicts, similar to Fig. 2, the single-epoch estimated horizontal North and East positioning errors, but now based on the 48 h of real multi-GNSS data and when compared to very precise benchmark coordinates. These benchmark coordinates were obtained by averaging all single-epoch estimated coordinates derived from assuming the ambiguities to be time-constant over the whole observation time span, while combining all four systems (c.f. Fig. 6), so as to maximize the model strength with a 100% ILS SR. Again, we make use of a zoom-in window to depict the two-order of magnitude improvement going from float to correctly fixed ILS solutions. To vary the ILS SRs, we look at different positioning models, with top left to bottom right panels depicting the results for an L1 GPS model and an elevation cut-off angle of 20°, but we remove four random GPS satellites here to make the model weaker. This follows by L1 GPS (20° cut-off without removing satellites), L1 GPS (cut-off 10°), L1 + E1 GPS + Galileo (cut-off 20°), L1 + E1 + L1 GPS + Galileo + QZSS (cut-off 20°), and L1 + E1 + B1 + L1 GPS + Galileo + BDS + QZSS (cut-off 20°), respectively. The ILS SR was computed by comparing the single-epoch estimated ambiguities to a set of reference ambiguities. These reference ambiguities were obtained by using a four-system model, with ambiguities again kept time-constant over the entire time-span, while the precise baseline and the satellite coordinates, as obtained from the broadcast ephemerides, are used so as to fix a known range. This is referred to as the 'geometry-fixed' model. Note that since we are now using a time-varying satellite geometry (c.f. Fig. 6) and much fewer epochs, the incorrectly ILS positioning solutions will not be clustered as heavily into similar locations like Fig. 2 (with a fixed satellite geometry). Figure 8 shows the corresponding histograms for the North positioning errors, where the East and Up component behave in a similar manner and are thus not shown for brevity.

Figure 7 confirms the simulation results in the previous section where the low ILS SRs, at the top row, give BIE solutions (green dots) that resemble or are better than the float solutions (black dots underneath or near the green dots), whereas when the model gets stronger at the middle and bottom panels the BIE solutions outperform the ambiguity-float counterparts. This is confirmed by inspecting the corresponding histograms in Fig. 8. Moreover, we see again a slight tendency of a star-like scattering of the BIE solutions, particularly at the bottom left panel with the 3-system model and an ILS SR of 99.3% similar to Fig. 2. However, due to the time-varying satellite geometry, this is now less pronounced. We can also see that there are several ILS solutions that are further away from zero meters than BIE, which is further evident by inspecting the corresponding histograms in Fig. 8. For instance, for the SF GPS + Galileo model (ILS SR 96.9%) at the third row of Fig. 8 and in the zoom-in window we can see several ILS North positioning errors above 2.5 m, whereas the number of such solutions is much fewer for BIE.

Figure 9 shows, similar to Fig. 5, the MSEs ratios of BIE as green and ILS as a dashed magenta line, relative to the ambiguity-float solutions, and with the float versus float ratio given as a black line. Since the estimated positions are unbiased, the MSEs equal the sum of the variances of North, East and Up.

Figure 9 shows that ILS has indeed a larger MSE than the float solutions for an ILS SR up to about 40%, which is remarkably similar to the simulation results in Fig. 5 where this happens at a ILS SR of about 45%. We can also see that the MSE of ILS is always larger than BIE until we reach an ILS SR of 100% (when they become similar). Finally, the MSE of BIE is always better than that of the float and ILS-fixed solutions (except for the 0% and 100% ILS SR cases, respectively).

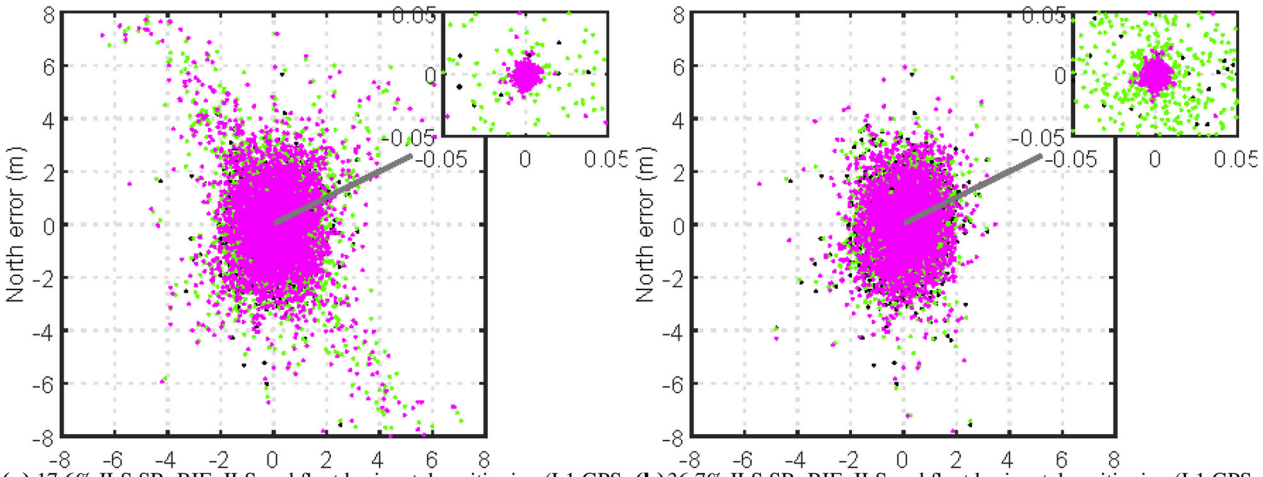

(a) 17.6% ILS SR: BIE, ILS and float horizontal positioning (L1 GPS, 20°, 4 removed satellites)

(b) 36.7% ILS SR: BIE, ILS and float horizontal positioning (L1 GPS, 20°)

(c) 75.7% ILS SR: BIE, ILS and float horizontal positioning (L1 GPS, 10°)

(d) 96.9% ILS SR: BIE, ILS and float horizontal positioning (L1+E1 GPS+Galileo, 20°).

(e) 99.3% ILS SR: BIE, ILS and float horizontal positioning (L1+E1+L1 GPS+Galileo+QZSS, 20°)

(f) 100.0% ILS SR: BIE, ILS and float horizontal positioning (L1+E1+B1+L1 GPS+Galileo+BDS+QZSS, 20°)

Fig. 7 Horizontal (North/East) scatter of the real multi-GNSS data derived BIE (*green dots*), ILS (*magenta dots*) and ambiguity-float (*black dots*) ionosphere-fixed SF RTK positioning for a 670 m baseline in Dunedin, NZ, based on two days of data (48 h, 30 s measurement interval) and ublox EVK-M8T + patch antennas. The corresponding histograms are depicted in Fig. 8

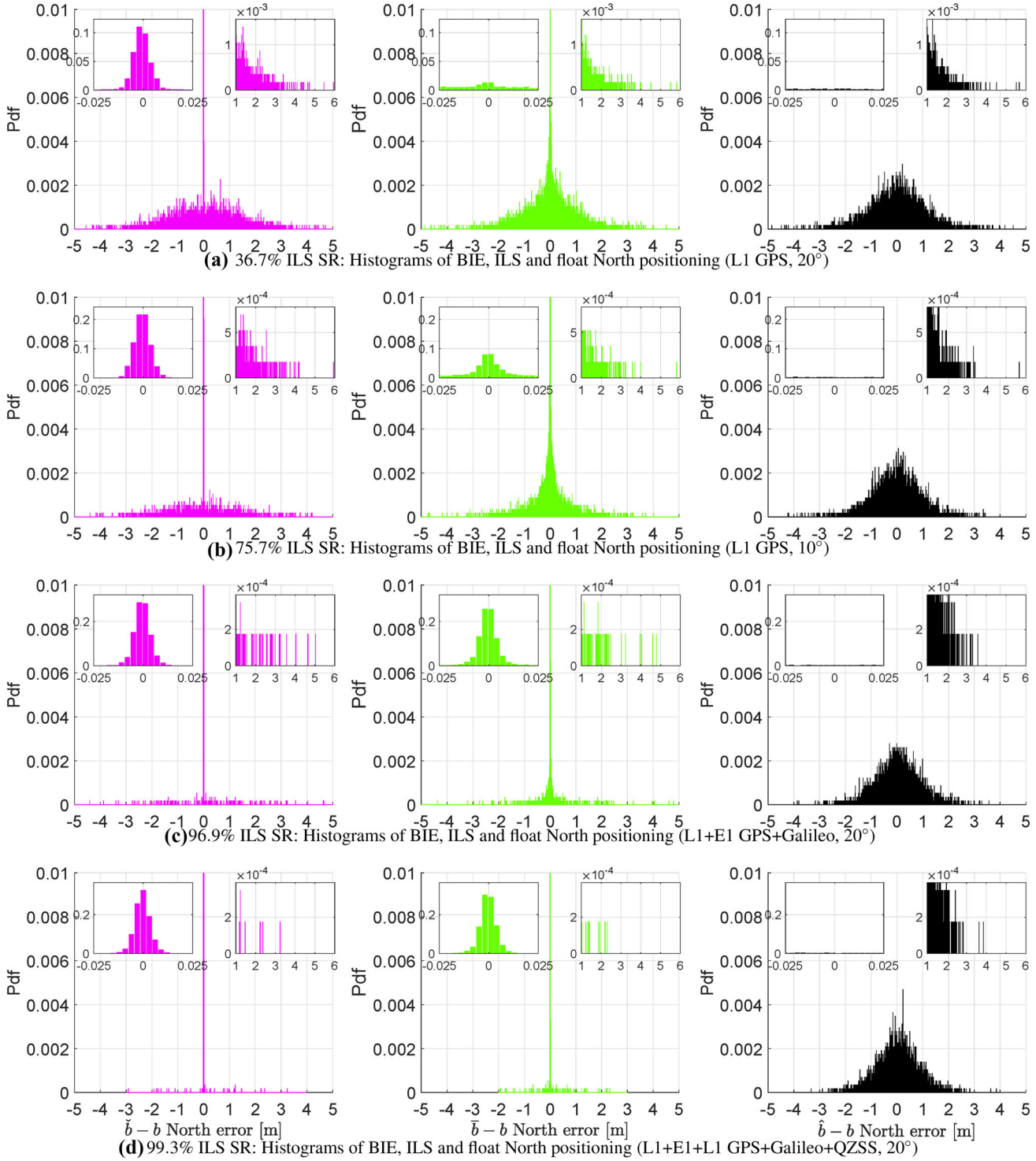

(a) 36.7% ILS SR: Histograms of BIE, ILS and float North positioning (L1 GPS, 20°)

(b) 75.7% ILS SR: Histograms of BIE, ILS and float North positioning (L1 GPS, 10°)

(c) 96.9% ILS SR: Histograms of BIE, ILS and float North positioning (L1+E1 GPS+Galileo, 20°)

(d) 99.3% ILS SR: Histograms of BIE, ILS and float North positioning (L1+E1+L1 GPS+Galileo+QZSS, 20°)

Fig. 8 Example histograms (bin size of 3 mm) of the real multi-GNSS data derived North positioning errors in Fig. 7 of the BIE (*green bars*), ILS (*magenta bars*), and ambiguity-float (*black bars*) solutions. The East and Up positioning histograms behave in a similar manner and are thus not shown for brevity. The zoom-in windows depict the spread of the sample solutions of North errors between −0.025 and 0.025 m and 1.0 to 6.0 m, respectively

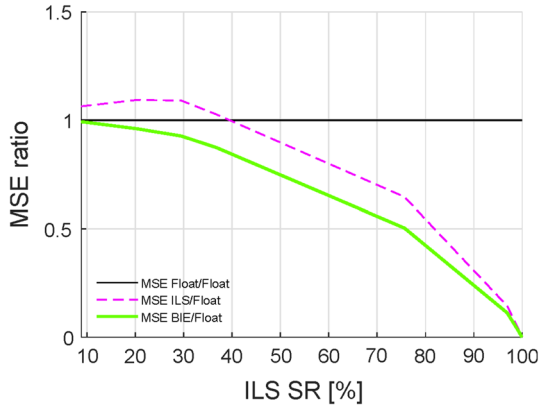

Fig. 9 MSE ratios of the ionosphere-fixed (670 m baseline, ublox + patch) SF single-epoch RTK positioning errors in Fig. 7, with BIE (*green line*), ILS (*dashed magenta line*), ambiguity-float (*black line*), all versus float

4 BIE for multi-epoch and long-baseline DF RTK positioning

In this section, we will extend our BIE simulation and real data analysis from the SF short baseline model, to a model when the relative atmospheric delays need to be modeled as completely unknown parameters with a DF model (here referred to as the 'ionosphere-float' model). The 112.9 km baseline and the two receiver types that will be analyzed are depicted in Fig. 10. The low-cost ublox ZED-F9P DF receivers are connected to low-cost ANN-MB patch antennas, and the survey-grade Trimble R10 receivers have integrated antennas. A circular ground plane was again used for each patch antenna. We ignore any phase center offset (PCO) and phase center variations (PCV) for the ANN-MB antennas, but emphasize that it could improve the ublox long-baseline results with a few millimeters (Krietemeyer et al. 2020).

Figure 11 depicts the total number of satellites during a 3 h period of the two receiver types in Fig. 10, with GPS as blue, BDS as magenta, Galileo as green and the 3-system model as a black line. Top row shows the number of satellites tracked by the DF ublox F9P model, whereas bottom row shows the corresponding number of satellites for the Trimble R10 receiver setup. We remark that the F9P receivers did not track BDS geostationary (GEO) satellites and tracked the civil GPS signals (L1C and L2C, see Nie et al. 2020), which restricts the total number of satellites for the model. We also note that the F9P receivers were able to track the QZSS L1 and L2 signals, however, due to a firmware issue at our end for one of the Trimble R10 receivers we were not able to track those satellites. Hence, we excluded QZSS for all receivers so that the results can be more fairly compared.

LS-VCE is again used to determine the stochastic model. We focus on determining the diagonal terms, whereas estimation of covariances between code/phase, frequencies and satellites was here neglected for brevity. Table 3 depicts the undifferenced and zenith-referenced code/phase STDs for ublox and Trimble R10 receivers/antennas. These results were all obtained for the 3 m baseline in the top right column of Fig. 10, while still taking into account the GPS satellite constellation repeatability period of one sidereal day (Axelrad et al. 2005). This so that the GPS STDs can be compared between the receivers, whereas the BDS medium earth orbit (MEO) and Galileo satellites do not have the same repeatability period.

Table 3 shows remarkable results for the ublox F9P receivers. For example, the C1C code STD of 18 cm is even better than the Trimble R10 receiver corresponding STD of 20 cm. When we inspected the DD code least squares residuals from which the ublox code STDs were obtained, we could see a smooth behavior which might indicate that some receiver-related filtering (possibly 'phase smoothing') is used for the ublox receivers. This is similar to the findings in Odolinski and Teunissen (2017b) for the corresponding ublox M8T SF receivers. When investigating the corresponding observation time correlation for a zero baseline setup, we found significant autocorrelation coefficients (Amiri-Simkooei and Tiberius 2007; Teunissen and Amiri-Simkooei 2008) over several seconds. Therefore, in the BIE real-data analysis, we will use a measurement interval of 10 s to largely avoid any such code time correlation.

4.1 BIE simulation for multi-epoch and long-baseline DF GPS RTK positioning

We are now ready to investigate the BIE performance for a long-baseline DF setup. Similarly to the short-baseline simulation results, we make use of Monte Carlo simulations, where again the GPS broadcast ephemerides and very precise benchmark coordinates are used. However, in this case we make use of the satellite visibility of the two Trimble R10 receivers forming a 112.9 km baseline in Fig. 10, and DF L1,L2 observations. The code and phase observations are again produced using the zenith-referenced and undifferenced STDs. In the single-baseline RTK model (1) and in addition to the baseline coordinates in b, we determine slant ionospheric delays and the relative (wet) zenith tropospheric delay (ZTD). Since atmospheric delays are present, we need to also extend our model from single-epoch to multi-epochs, i.e., we use a dynamic model for certain parameters in a Kalman filter. The ambiguities are kept time-constant, and for the relative ZTD, we use a random walk process noise of $2\,\mathrm{mm}/\sqrt{\mathrm{h}}$ similarly to (Odolinski et al. 2014, 2015), whereas all other parameters are treated as unlinked in time.

The DF GPS satellite constellation used is depicted in Fig. 12, with the same number of satellites to the short-baseline data (Fig. 1), and in total we simulate 10,000 samples

(a) Receiver setup of 112.9 km baseline

(b) ublox F9P+ANN-MB (*left*), and Trimble R10 (*right*)

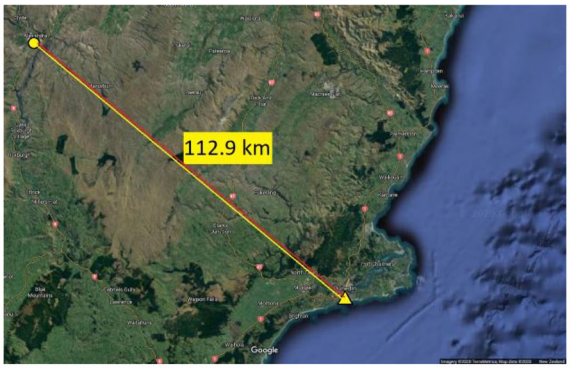

(c) 112.9 km baseline to be analyzed for DF RTK positioning

Fig. 10 Baseline of 112.9 km between Dunedin (WGS84 latitude 45.87° S, longitude 170.511° E) to Alexandra (latitude 45.25° S, longitude 169.377° E): GNSS RTK receivers collecting data for single-baseline RTK (1) during 3 h at 19 Feb, 2019 at 18:12:00 to 21:12:00 (hh:mm:ss) UTC. **a** Patch ANN-MB antennas are connected to the two **b** ublox ZED-F9P receivers (forming one low-cost baseline), and the two Trimble R10 receivers have their own integrated antennas (forming a survey-grade baseline). The map in **c** was obtained through Map data ©Google

of observations for each epoch in the Kalman filter. We found that adding many more samples of observations did not significantly change the following results.

Figure 13 shows the MSE ratios as a function of time for the simulated 3D positioning errors. In addition, we depict as a gray line the ILS SR. Figure 13 shows, similarly to Fig. 5, that the ILS estimator becomes better than the float estimator at an ILS SR of about 45%. Since we are now using a long-baseline with atmospheric delays present and a DF GPS model, this takes more than 10 epochs. Most importantly, the BIE estimator is, as expected, at least equal to float for single-epoch positioning, and better than the float estimator when a multi-epoch model is employed. BIE is also better than ILS for all epochs until the ILS SR reaches a value of 100% at 40 epochs, when they become equal.

4.2 BIE for multi-epoch and long-baseline DF RTK positioning with real multi-GNSS data

In this section, we will evaluate a snapshot of the real data collected through the long-baseline (112.9 km) experiment in Fig. 10 while using low-cost ublox F9P receivers connected to low-cost ANN-MB patch antennas. The results will be compared to that of survey-grade Trimble R10 receivers with their integrated antennas. The DIA (Teunissen 1990) is again used to detect and identify outliers such as cycle slips.

We depict in Table 4 the time to first fix (TTFF) of the two receiver models while using 3 h (10 s) of data and an elevation cut-off angle of 10°. The TTFF is defined as the time when the horizontal positioning errors go below and stay below 0.15 m. The Up component is not shown for brevity as it shows little improvement by ambiguity-fixing similar to Odijk et al. (2017). These positioning errors were computed by comparing the estimated positions to very precise bench-

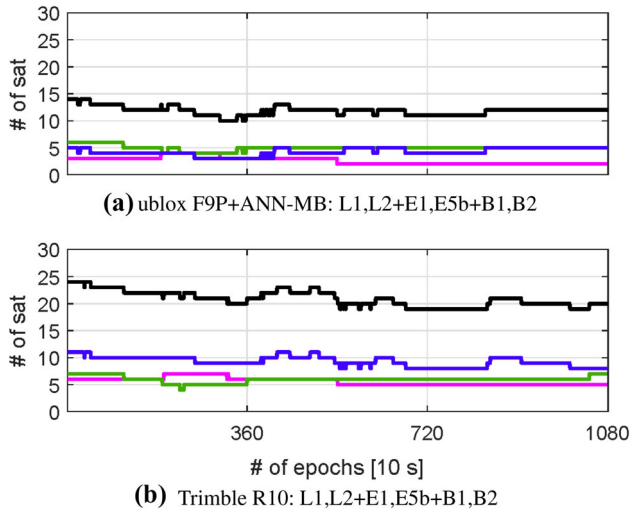

Fig. 11 Number of satellites for DF GPS + Galileo + BDS with an elevation cut-off angle of 10° for the real multi-GNSS data collected in Dunedin and Alexandra, NZ (Fig. 10), with ublox F9P + ANN-MB (*top row*) and Trimble R10 (*bottom row*). The *black lines* corresponds to a combined 3-system model, *blue lines* GPS, *green lines* Galileo and *magenta lines* BDS. Note that the F9P receivers did not track BDS GEO satellites and tracked only the civil GPS signals (L1C and L2C), which explains the difference in the number of tracked satellites to the Trimble R10 receivers

Table 3 Undifferenced and zenith-referenced STDs for code and phase for a DF GPS + Galileo + BDS model (ublox + ANN-MB and Trimble R10), with an elevation cut-off angle of 10° over 2 h (1 s) of real data collected for a 3 m baseline in Dunedin, NZ

Receiver/antenna	System	Frequency	$\hat{\sigma}_{p_j}$ (cm)	$\hat{\sigma}_{\phi_j}$ (mm)
Ublox F9P	GPS	C1C/L1C	18	2
+ANN-MB		C2C/L2C	18	2
	Galileo	E1	21	2
		E5b	10	2
	BDS	B1	34	2
		B2	11	2
Trimble R10	GPS	C1C/L1C	20	2
		C2W/L2W	25	2
	Galileo	E1	14	2
		E5b	10	2
	BDS	B1	29	2
		B2	17	2

The RINEX3 notation is used for the GPS frequencies, since the ublox receivers were restricted to civil GPS signals, whereas Trimble tracked all GPS satellites

mark coordinates. The benchmark coordinates were again obtained by averaging all single-epoch estimated coordinates derived from assuming the ambiguities to be time-constant (and ZTD treated with random walk process noise) over the whole observation time span, while combining all three systems. We make use of two re-initializations of the Kalman filter to compute the TTFF, one at the maximum number of

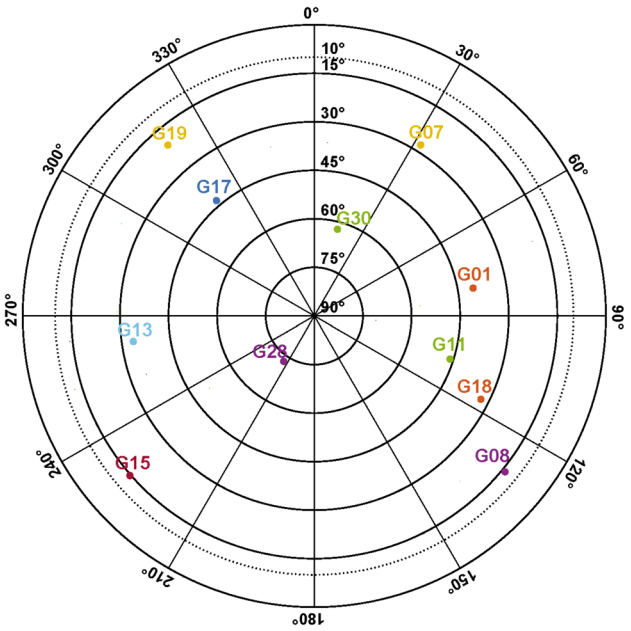

Fig. 12 Skyplot of L1,L2 GPS with an elevation cut-off angle of 10° for the simulated data for the long-baseline in Dunedin and Alexandra, NZ (c.f. Fig. 10)

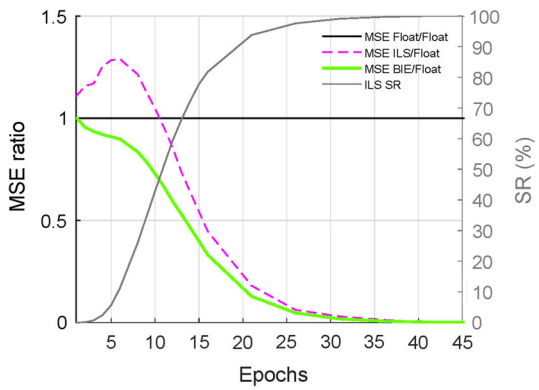

Fig. 13 MSE ratios of the simulated (10,000 samples, see Fig. 12) BIE (*green line*), ILS (*dashed magenta line*), ambiguity-float (*black line*) solutions, all versus float, for the ionosphere-float DF RTK positioning errors. The corresponding ILS SR is also depicted (*gray line*)

Trimble satellites at epoch one, and one initialization at the minimum number of Trimble satellites and halfway through the observation time span for the respective models. Note that the average number of satellites for ublox during the two initialization periods are about 14 and 12, respectively, whereas Trimble have corresponding 24 and 20 number of tracked satellites (c.f. Fig. 11). The corresponding ILS SRs for ublox and Trimble are 92.7% and 96.6%, respectively.

The snapshot results in Table 4 show that the ublox model requires an ILS and BIE TTFF of 37 epochs (6 min and 10 s) and 42 epochs (7 min), respectively. The Trimble model requires an ILS TTFF of 11 epochs (1 min and 50 s) and 26 epochs (4 min and 20 s), respectively, while BIE requires one

Table 4 Empirical STDs of ionosphere-float horizontal positioning errors and TTFF (# of epochs with 10 s measurement interval) defined as the time when the horizontal positioning errors for BIE, ILS and float are below and stay below 0.15 m

Model	Estimator	TTFF (1st init., 10 s)	TTFF (2nd init., 10 s)	STD before TTFF (m)	STD after TTFF (m)
DF ublox+ANN-MB	BIE	37 (# epochs)	42 (# epochs)	0.368	0.010
L1+L2,E1+E5b,B1+B2	ILS	37 (# epochs)	42 (# epochs)	0.429	0.009
	Float	143 (# epochs)	177 (# epochs)	0.382	0.102
Trimble R10	BIE	12 (# epochs)	27 (# epochs)	0.168	0.014
L1+L2,E1+E5b,B1+B2	ILS	11 (# epochs)	26 (# epochs)	0.202	0.012
	Float	197 (# epochs)	77 (# epochs)	0.181	0.092

This is based on two re-initializations of the Kalman filter at epoch one (with maximum number of Trimble satellites) and halfway through the observation time period at epoch 541 (with minimum number of Trimble satellites), c.f. Fig. 11. The STDs are given before the minimum TTFF (ILS) and after this TTFF, so that the STDs can be fairly compared between estimators as they are then based on the same number of epochs. This is given for two 112.9 km baselines based on DF ublox and Trimble R10 receivers, respectively. An elevation cut-off angle of 10° is used and 3 h of data (Fig. 10)

additional epoch for the two initializations. In other words, the ILS TTFF difference is a mere 2 min and 40 s during the second initialization between the low-cost ublox and survey-grade Trimble model. It is also shown that the TTFF for both ILS and BIE is much shorter than for the float solutions for both receiver types. For instance, the ublox model reaches BIE and ILS TTFF after 37 epochs (6 min and 10 s) during the first initialization, while the float solutions have a TTFF of 143 epochs (23 min and 50 s).

The empirical STDs in Table 4 are based on the horizontal errors that were obtained by comparing the estimated coordinates to the benchmark coordinates. These empirical STDs are for all estimators computed before the minimum TTFF, as derived from ILS, and also after this TTFF. This is done so that the corresponding STDs can be fairly compared between estimators as they are then based on the same number of epochs. If we inspect Table 4, this means that the empirical STDs before TTFF for all estimators (column five) and ublox are based on horizontal errors with epoch intervals consisting in total of 36 epochs and 41 epochs, respectively. This is when the TTFF criterion of horizontal errors below 0.15 m has not yet been obtained for ILS and the two Kalman filter re-initializations. The corresponding STDs for Trimble are based on intervals consisting of 10 epochs and 25 epochs, respectively. The empirical STDs after TTFF (column six) are then based on all other epochs when the TTFF criterion of horizontal errors below 0.15 m has been obtained for ILS.

In order to understand the magnitude of the empirical STDs in Table 4 better, we provide here an explanation. Before TTFF and at the beginning of the two Kalman filter initializations, the float ambiguities will be less precise and the code observations will dominate the precision of the baseline components. This will then result in low to medium ambiguity SRs and sub-meter level empirical STDs for the horizontal errors (column five in Table 4). On the other hand, once the ambiguities are of a sufficiently good precision, one can with ILS successfully fix the ambiguities to their correct integer values and quickly reach the TTFF criterion. All horizontal errors after the TTFF will then be driven by the very precise carrier-phase data, and high ambiguity SRs, until the second Kalman filter re-initialization and its TTFF. This explains the sudden decrease in the float STDs before TTFF to relatively precise values after TTFF (column six in Table 4), and that the BIE STDs become very similar to the ones obtained by ILS after TTFF indeed. Table 4 reveals that the horizontal STDs after TTFF are still much better for both BIE and ILS when compared to the float solution. For instance, the ublox model has corresponding BIE and ILS STDs of 0.010 m and 0.009 m, respectively, while the float solutions have a STD of 0.102 m. The poorer performance for the float estimator is attributed to the longer time it takes to reach cm-level positioning precisions (see also the TTFFs).

Also note that the Trimble TTFF for the float solution and the first initialization is 197 epochs, whereas for the second initialization it is 77 epochs. This is in contrast to what one would have expected considering the total number of satellites used (Fig. 11). As a matter of fact, the float solution goes below the 0.15 m level quicker at the first initialization in comparison with the second initialization. However, due to satellites that sets (and rises again) when this has occurred (c.f. Fig. 11), the float horizontal solution increases in error again and exceeds again the 0.15 m threshold. This has as a consequence that it does not fulfill our TTFF criterion of being below 0.15 m until after 197 epochs.

Finally, we can see in Table 4, in analogy to the simulation results, that when the SR is too low for successful fixing and hence TTFF has not yet been obtained, BIE outperforms both the ILS and float solutions. This is shown by the smaller BIE horizontal STDs (column five in Table 4) for both ublox and Trimble being 0.368 m and 0.168 m, respectively, whereas the corresponding ILS STDs are 0.429 m and 0.202 m. The float STDs are here also poorer than the BIE estimator, with values of 0.382 m and 0.181 m for ublox and Trimble, respectively.

5 Conclusions

In this contribution, we evaluated the approximation of the best integer equivariant (BIE) estimator (10), which can be preferred over the float solution when the integer success rate (SR) is different from one. This since BIE estimation will always be better in the minimum mean squared error (MMSE) sense than the float and integer least squares (ILS) solutions. We evaluated the BIE single-baseline RTK performance through Monte Carlo simulations and compared the results to multi-GNSS, single-frequency (SF) and dual-frequency (DF) low-cost receiver and antenna data collected in Dunedin, New Zealand. With 'low-cost', we refer to a cost of at most a few hundred USDs for the receiver and antenna. Our results were evaluated for a short- (670 m) and a long-baseline (112.9 km), where the relative atmospheric delays can be neglected and need to be estimated, respectively. In our model (1), we distinguished between the single-epoch case for the short-baseline, to using multiple epochs and a Kalman filter with a dynamic model when the long-baseline was used. We also compared the multi-GNSS positioning performance of the low-cost receiver model to that of survey-grade receivers and antennas.

First, we used Monte Carlo simulations to simulate observations of a SF single-epoch GPS model, while assuming the relative atmospheric delays to be absent. Single-epoch positioning errors were estimated by comparing the BIE, ILS and float estimated positions to the known benchmark coordinates, and we simultaneously estimated the single-epoch ILS SRs. The simulation results were subsequently compared to that of L1 GPS, E1 Galileo, B1 BDS and L1 QZSS ublox EVK-M8T data. It was demonstrated that the BIE positioning performance is better than that of the float and ILS solutions when the ILS SR is at low to medium levels, where one would not fix the ambiguities to integers in practice. When the ILS SRs were close to 0% and 100%, respectively, the BIE performance was shown to be similar to that of the float and ILS solution, respectively. We also demonstrated the distributional properties of BIE positioning, where it was shown that a 'star-like' pattern reveals itself once the model gets stronger and the ILS success rate increases.

We then investigated the simulated long-baseline DF BIE performance of L1,L2 GPS and the real data of a 112.9 km baseline, while employing L1,L2 GPS, B1, B2 BDS and E1, E5b Galileo data. The performance was compared between the low-cost ublox ZED-F9P receivers connected to patch ANN-MB antennas, and survey-grade Trimble R10 receivers and antennas. While using the long-baseline, multiple epochs were needed for precise positioning, and the simulation showed again that BIE outperformed ILS and the float solutions for ILS SRs at low to medium levels. We then evaluated the time to first fix (TTFF) based on the 112.9 km baseline and DF multi-GNSS data, which was defined as the time when the horizontal positioning errors go below and stay below 0.15 m. It was concluded that the survey-grade DF Trimble solution performed slightly better than the DF ublox receivers and antennas. We finally showed that the BIE performance is better than both ILS and float before TTFF, and similar to that of ILS after successful fixing.

With the above BIE performance studies, we have presented results based on real data collected by low-cost multi-GNSS receivers using the single-baseline RTK model for both short and long baselines. More studies can be considered, such as those for network-RTK and Precise Point Positioning (PPP) RTK.

Acknowledgements Kade Phillips, School of Surveying, collected the GNSS data. The National Institute of Water & Atmospheric Research (NIWA) in Alexandra, NZ, allowed us to conduct a GNSS experiment at their property. The second author is the recipient of an Australian Research Council (ARC) Federation Fellowship (Project Number FF0883188). All this support is gratefully acknowledged.

Author contributions The first author R. Odolinski performed the research, wrote the manuscript and did the data analysis. P. J. G. Teunissen gave feedback on the written manuscript and wrote some of the theoretical parts of the paper.

Data availability The broadcast ephemerides were used for satellite orbits and clocks. The low-cost and survey-grade receiver observation data are stored at University of Otago and the School of Surveying data facilities, and can be made available upon request by contacting the corresponding author R. Odolinski by email.

References

Aggrey J, Bisnath S, Naciri N, Shinghal G, Yang S (2020) Multi-GNSS precise point positioning with next-generation smartphone measurements. J Spat Sci 65(1):79–98. https://doi.org/10.1080/14498596.2019.1664944

Amiri-Simkooei AR, Tiberius CCJM (2007) Assessing receiver noise using GPS short baseline time series. GPS Solut 11(1):21–35

Axelrad P, Larson K, Jones B (2005) Use of the correct satellite repeat period to characterize and reduce site-specific multipath errors. In: Proceedings of ION GNSS 18th international technical meeting of the satellite division, Long Beach, CA

Brack A (2015) On reliable data-driven partial GNSS ambiguity resolution. GPS Solut 19(4):411–422

Brack A (2017) Reliable GPS + BDS RTK positioning with partial ambiguity resolution. GPS Solut 21:1083–1092

Brack A (2019) Partial carrier-phase integer ambiguity resolution for high accuracy GNSS positioning. PhD dissertation, Lehrstuhl fur Kommunikation und Navigation Technische Universitat Munchen

Brack A, Gunther C (2014) Generalized integer aperture estimation for partial GNSS ambiguity fixing. J Geod 88(5):479–490

Brack A, Henkel P, Gunther C (2014) Sequential best integer-equivariant estimation for GNSS. Navigation 61(2):149–158

De Jonge PJ, Tiberius CCJM (1996) The LAMBDA method for integer ambiguity estimation: implementation aspects. LGR-Series, technical report, Delft University of Technology (12)

Euler HJ, Goad C (1991) On optimal filtering of GPS dual frequency observations without using orbit information. Bull Geod 65:130–143

Krietemeyer A, van der Marel H, van de Giesen N, ten Veldhuis MC (2020) High quality zenith tropospheric delay estimation using a low-cost dual-frequency receiver and relative antenna calibration. Remote Sens 12:1393

Laurichesse D, Banville S (2018) Instantaneous centimeter-level multi-frequency precise point positioning. GPS World, Innovation column 4 July

Mongredien C, Doyen JP, Strom M, Ammann D (2016) Centimeter-level positioning for UAVs and other mass-market applications. In: ION GNSS, Portland, Oregon

Nie Z, Liu F, Gao Y (2020) Real-time precise point positioning with a low-cost dual-frequency GNSS device. GPS Solut. https://doi.org/10.1007/s10291-019-0922-3

Odijk D, Teunissen PJG (2013) Characterization of between-receiver GPS–Galileo inter-system biases and their effect on mixed ambiguity resolution. GPS Solut 17(4):521–533

Odijk D, Khodabandeh D, Nadarajah N, Choudhury M, Zhang B, Li W, Teunissen PJG (2017) PPP-RTK by means of Ssystem theory: Australian network and user demonstration. J Spat Sci 62(1):3–27. https://doi.org/10.1080/14498596.2016.1261373

Odolinski R, Teunissen PJG (2016) Single-frequency, dual-GNSS versus dual-frequency, single-GNSS: a low-cost and high-grade receivers GPS-BDS RTK analysis. J Geod 90(11):1255–1278. https://doi.org/10.1007/s00190-016-0921-x

Odolinski R, Teunissen PJG (2017a) Low-cost, 4-system, precise GNSS positioning: a GPS, Galileo, BDS and QZSS ionosphere-weighted RTK analysis. Meas Sci Technol. https://doi.org/10.1088/1361-6501/aa92eb

Odolinski R, Teunissen PJG (2017b) Low-cost, high-precision, single-frequency GPS-BDS RTK positioning. GPS Solut 21(3):1315–1330. https://doi.org/10.1007/s10291-017-0613-x

Odolinski R, Teunissen PJG (2019) An assessment of smartphone and low-cost multi-GNSS single-frequency RTK positioning for low, medium and high ionospheric disturbance periods. J Geod 93:701–722. https://doi.org/10.1007/s00190-018-1192-5

Odolinski R, Teunissen PJG, Odijk D (2013) Quality analysis of a combined COMPASS/BeiDou-2 and GPS RTK positioning model. In: IGNSS symposium, Golden Coast, Australia

Odolinski R, Teunissen PJG, Odijk D (2014) Combined GPS + BDS + Galileo + QZSS for long baseline RTK positioning. In: ION GNSS, Tampa, Florida, USA

Odolinski R, Teunissen PJG, Odijk D (2015) Combined GPS + BDS for short to long baseline RTK positioning. Meas Sci Technol 26:045801. https://doi.org/10.1088/0957-0233/26/4/045801

Paziewski J, Sieradzki R, Radoslaw B (2019) Signal characterization and assessment of code GNSS positioning with low-power consumption smartphones. GPS Solut. https://doi.org/10.1007/s10291-019-0892-5

Riley S, Lentz W, Clare A (2017) On the path to precision—observations with android GNSS observables. In: Proceedings of ION GNSS, Portland, Oregon

Teunissen PJG (1990) An integrity and quality control procedure for use in multi sensor integration. In: Proceedings of the 3rd international technical meeting of the satellite division of the institute of navigation (ION GPS 1990), Colorado Spring, CO, pp 513–522, also published in: volume VII of the GPS red book: integrated systems, ION Navigation, 2012

Teunissen PJG (1995) The least squares ambiguity decorrelation adjustment: a method for fast GPS integer estimation. J Geod 70:65–82

Teunissen PJG (1999a) An optimality property of the integer least-squares estimator. J Geod 73:587–593

Teunissen PJG (1999b) The probability distribution of the GPS baseline for a class of integer ambiguity estimators. J Geod 73(5):275–284

Teunissen PJG (2003a) Adjustment theory—an introduction. Series on mathematical geodesy and positioning. Delft University Press, Delft

Teunissen PJG (2003b) Theory of integer equivariant estimation with application to GNSS. J Geod 77:402–410. https://doi.org/10.1007/s00190-003-0344-3

Teunissen PJG (2005) On the computation of the best integer equivariant estimator. Artif Satell 40(3):161–171

Teunissen PJG, Amiri-Simkooei AR (2008) Least-squares variance component estimation. J Geod 82(2):65–82

Teunissen PJG, Verhagen S (2009) The GNSS ambiguity ratio-test revisited: a better way of using it. Surv Rev 41(312):138–151

Teunissen PJG, Joosten P, Tiberius CCJM (1999) Geometry-free ambiguity success rates in case of partial fixing. In: Proceedings of ION ITM, San Diego, CA, USA, pp 201–207

Verhagen S (2005) The GNSS integer ambiguities: estimation and validation. PhD dissertation, Netherlands Geodetic Commission, Publications on Geodesy, 58

Verhagen S, Teunissen PJG (2005) Performance comparison of the BIE estimator with the float and fixed GNSS ambiguity estimators. In: A window on the future of geodesy, international association of geodesy symposia, vol 128. Springer, Berlin, Heidelberg, pp 428–433

Wand MP, Jones M (eds) (1995) Kernel smoothing. Chapman and Hall, London

Yang Y, Li J, Wang A, Xu J, He H, Guo H, Shen J, Dai X (2014) Preliminary assessment of the navigation and positioning performance of BeiDou regional navigation satellite system. Sci China Earth Sci 57:144–152

Yang Y, Gao W, Guo S, Mao Y, Yang Y (2019) Introduction to BeiDou-3 navigation satellite system. Navigation 66:7–18

Zhang X, Tao X, Zhu F, Shi X, Wang F (2018) Quality assessment of GNSS observations from an Android N smartphone and positioning performance analysis using time differenced filtering approach. GPS Solut. https://doi.org/10.1007/s10291-018-0736-8